

## Scattering matrices of martian dust analogs at 488 nm and 647 nm



Dominika D. Dabrowska<sup>a</sup>, Olga Muñoz<sup>a,\*</sup>, Fernando Moreno<sup>a</sup>, José L. Ramos<sup>a</sup>, Jesús Martínez-Frías<sup>b</sup>, Gerhard Wurm<sup>c</sup>

<sup>a</sup> Instituto de Astrofísica de Andalucía, CSIC, Glorieta de Astronomía S/N, 18008 Granada, Spain

<sup>b</sup> Instituto de Geociencias, UCM-CSIC, C/José Antonio Novais, 12, 28040 Madrid, Spain

<sup>c</sup> Fakultät für Physik, Universität Duisburg-Essen, Lotharstrasse 1, 47057 Duisburg, Germany

### ARTICLE INFO

#### Article history:

Received 16 July 2014

Revised 29 October 2014

Accepted 21 November 2014

Available online 2 December 2014

#### Keywords:

Experimental techniques

Mars, atmosphere

Polarimetry

### ABSTRACT

We present measurements of the complete scattering matrix as a function of the scattering angle of five martian dust analogs, namely montmorillonite, two palagonite (JSC-1) samples, basalt, and calcite. The measurements are performed at 488 and 647 nm, covering the scattering angle range from 3° to 177°. The experimental scattering matrices are compared with results of Lorenz–Mie calculations performed for the same size distributions and refractive indices as our analog samples. As expected, we find that scattering matrices of realistic polydispersions of dust particles cannot be replaced by such calculated matrices. In contrast, the measured phase functions for our martian dust analogs may be considered a good approximation for martian dust at the studied wavelengths. Further, because of the sensitivity of polarimetry to particle microphysics, spectro-polarimetric observations from the martian surface appear to be a powerful diagnostic tool to infer the composition of the dust in the martian atmosphere. To facilitate the use of the experimental matrices for multiple-scattering calculations with polarization included, we compute the corresponding synthetic scattering matrices based on the measurements and defined in the full angle range from 0° to 180°.

© 2014 Elsevier Inc. All rights reserved.

## 1. Introduction

Martian atmospheric dust plays a crucial role in the planet's radiative transfer budget. Dust particles can modify the temperature, dynamics, and chemical composition of the atmosphere. Indeed, the importance of the studies of the spatial and temporal distribution of dust, its optical properties, and its influence on climate on Mars, have motivated a number of space missions to the planet. Still, the quantification of the influence of dust particles on the atmosphere of Mars is far from trivial.

In the first place, the dust distribution is highly variable in time and location on the planet, owing to the occurrence of a variety of transport phenomena, ranging from small-scale thermal eddies to global dust storms. Several mechanisms are postulated to lift dust particles from martian surface. Apart from horizontal winds in the lowest atmospheric layers, solid state greenhouse effects or photo-phoresis have been proposed (e.g. Wurm and Krauss, 2006; Wurm et al., 2008). Moreover, de Beule et al. (2014) have recently shown that martian soil can work as a gas (Knudsen) pump injecting the particles into the atmosphere.

In the second place, dust grains are irregular in shape, as confirmed by the Phoenix Lander microscope images (e.g. Smith

et al., 2009). This introduces a serious difficulty in the radiative transfer modeling. While the treatment of the scattering processes from spherical dust particles is straightforward using Lorenz–Mie theory, it is extremely tedious, or even impossible, for realistic polydispersions of non-spherical particles. One reason is the large memory and CPU needed by the available light scattering codes to compute the scattering matrix for individual irregular particles with sizes of the order or larger than the wavelength of the incident light (e.g. Mishchenko et al., 1996, 2000; Draine and Flatau, 2003; Kahnert, 2003; Taflove and Hagness, 2005; Yurkin and Hoekstra, 2007; Muinonen et al., 2009; Wriedt, 2009). Another reason is the difficulty in properly representing the internal structure and surface roughness of those particles as seen in nature (Muinonen et al., 2009).

In many cases, in radiative transfer calculations, the vector nature of light is replaced by its intensity or flux, i.e. polarization is ignored. We might note that under multiple scattering conditions (as is the case during large dust storms on Mars) even in the cases when only the radiance need to be computed, adopting a scalar representation of light induces significant, wavelength dependent, errors in the calculated planetary phase functions and geometric albedos (Moreno et al., 2002; Stam and Hovenier, 2005). Thus, an appropriate representation of the scattering matrix of dust particles is mandatory under multiple scattering conditions. All in all,

\* Corresponding author.

measurements of the full scattering matrices (including polarization) of realistic polydispersions of dust particles in the laboratory remain an extremely valuable tool.

The light scattering properties of martian dust have been so far estimated from analysis of the light scattered or emitted by the atmosphere or by the contribution of atmosphere plus surface (e.g. Wolff et al., 2010; Clancy et al., 2003; Pollack et al., 1995; Tomasko et al., 1999; Lemmon et al., 2004). In this paper, we report on measurements of the full  $4 \times 4$  scattering matrix as a function of the scattering angle of five martian dust analogs. The measurements are performed at the IAA COsmic DUSt LABORatory (CODULAB) (Muñoz et al., 2010), at two different wavelengths (488 and 647 nm) covering the scattering angle range from  $3^\circ$  to  $177^\circ$ . In Section 2, we present an outline of the currently known properties of martian dust, and introduce the terrestrial samples that we use as martian analogs. Section 3 is devoted to the description of the light scattering setup CODULAB. Results and discussion of our experiments, comparison with Lorenz–Mie theory calculations, and the construction of the “synthetic” scattering matrices are given in Section 4. In Section 5, we compare our measurements with martian dust observations. Finally, the conclusions of the paper are drawn in Section 6.

## 2. Physical properties of martian dust and its terrestrial analogs

### 2.1. Martian dust properties

Mars Exploration Rovers (MER) Microscopic Imager observations have shown that surface dust occurs as fragile, low-density, sand-sized (200–300  $\mu\text{m}$ ) aggregates (Sullivan et al., 2008). In contrast, atmospheric dust is much finer, but probably similar in form to loose material on the surface. The Phoenix microscopic images confirmed the irregular shapes of the airborne dust.

Space-based observations with OMEGA, a visible and infrared mineralogical mapping spectrometer on board Mars Express Orbiter, have shown a high abundance of iron oxides in the dusty bright regions of the planet (Poulet et al., 2007). The typical soil (Gusev Crater, Meridiani Planum and Gale Crater) is dominated by silicon dioxide  $\text{SiO}_2$  and ferric oxide  $\text{FeO}$  (Yen et al., 2013). Results from the Mars Pathfinder mission indicate that atmospheric dust is composed of micron-sized silicate particles composed in part of different ferric minerals. Different surface missions present slightly different soil composition (Yen et al., 2013). This indicates that

the dust has been largely homogenized but there is still a small influence of underlying geologic units. Because of past volcanic activity on Mars there are many basaltic rocks. Therefore, martian dust could be composed by basalt or its weathering product. Minor components of the dust have also been identified in the soils around the Phoenix landing site, such as calcium carbonate, which is a possible form of calcite, ikaite, aragonite, or ankerite (Boynton et al., 2009).

A crucial parameter of the dust is the complex refractive index,  $m = n + ik$  which is intimately related to the composition. Estimates of  $m$  are provided by e.g. Ockert-Bell et al. (1997), Tomasko et al. (1999), and Wolff et al. (2009, 2010). Their results approximately agree with each other (see Fig. 1). The real part,  $n$ , remains nearly constant from UV to IR having values ranging from 1.47 to 1.5. The imaginary part displays a severe decrease from values around  $k = 0.014$  at UV to 0.001–0.002 at red and near-IR wavelengths. At longer wavelengths,  $k$  increases moderately up to 0.006 at 2500 nm increasing drastically up to 0.05 at 2900 nm (Wolff et al., 2010). The exact retrieved values depend on model assumption, namely particle size distributions and phase functions used.

The size distribution is usually described by its effective radius,  $r_{\text{eff}}$  and effective variance,  $v_{\text{eff}}$  as defined by Hansen and Travis (1974):

$$r_{\text{eff}} = \frac{\int_0^\infty r \pi r^2 n(r) dr}{\int_0^\infty \pi r^2 n(r) dr} \quad (1)$$

$$v_{\text{eff}} = \frac{\int_0^\infty (r - r_{\text{eff}})^2 \pi r^2 n(r) dr}{r_{\text{eff}}^2 \int_0^\infty \pi r^2 n(r) dr} \quad (2)$$

Regarding particle size in the martian atmosphere, early results and retrieval methods were reviewed by Dlugach et al. (2003). They gave sizes retrieved from polarimetric observations ranging from very small particles ( $r_{\text{eff}}$  around 0.05  $\mu\text{m}$ ) during a high-transparency period to  $r_{\text{eff}} > 9 \mu\text{m}$  during Global Dust Storm conditions. Estimates of martian aerosol properties are obtained from sky images taken from the martian surface (Tomasko et al., 1999) and from emission phase function (EPF) observations by the Mars Global Surveyor (MGS) Thermal Emission Spectrometer (TES) (Clancy et al., 2003; Wolff and Clancy, 2003). Whereas the latter observations from the orbit give valuable overview of the dust in the entire atmosphere around the planet, the measurements made from the Mars surface represent the local dust properties of the lower atmosphere.

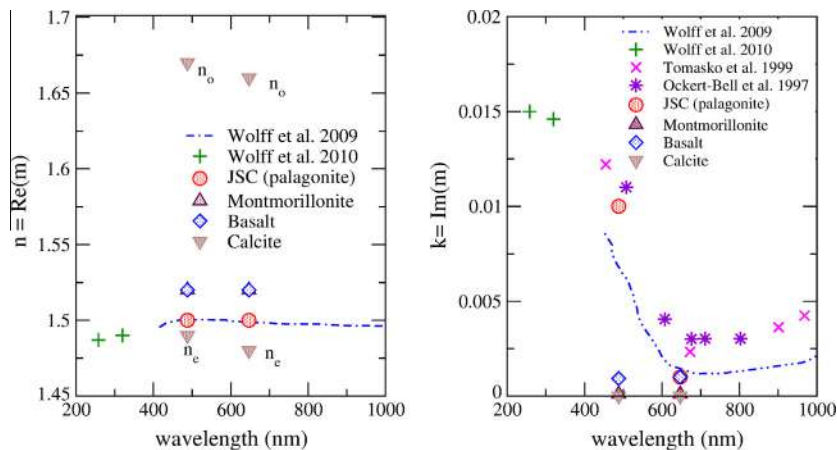


**Fig. 1.** Wavelength dependence of the real (left panel) and imaginary (right panel) parts of the refractive index for martian dust. The values in the 440 to 1000 nm range are adopted from Wolff et al. (2009). The 258 to 320 nm dependence is taken from Wolff et al. (2010). The values derived by Wolff et al. (2009) for the imaginary part of the refractive index are compared with previous work by Tomasko et al. (1999) and Ockert-Bell et al. (1997). The retrievals of martian dust are presented together with the refractive indices of our samples of martian dust analogs (Table 1). Please note that in the case of calcite, the ordinary,  $n_o$  and extraordinary,  $n_e$  refractive indices are shown. In Table 1 we present the effective refractive index of the sample.

Models of martian dust are consistent with the 1–2.5  $\mu\text{m}$  size range. The typical values during the 2001 Global Dust Storm range from 1.8 to 2.5  $\mu\text{m}$ , whereas 1  $\mu\text{m}$  is typical for quiet periods (Clancy et al., 2003). Under moderate dust loading conditions, Pollack et al. (1995), Tomasko et al. (1999), Lemmon et al. (2004) and Markiewicz et al. (1999), retrieved middle size airborne dust close to 1.5–1.6  $\mu\text{m}$  from surface-based observations at different visible wavelengths.

Apart from the weather conditions, the size of airborne martian dust depends on altitude. At high altitude, over 20 km, very fine particles of  $r_{\text{eff}} = 0.01 - 0.1 \mu\text{m}$  are found (Rannou et al., 2006). In contrast, strong winds near the surface tend to also catch large dust particles. Therefore, a variety of dust size distributions can be actually found in the atmosphere depending on the efficiency of dust lifting-up mechanisms. In general, the effective variance,  $v_{\text{eff}}$ , of martian dust size distribution is rather poorly constrained.

As a representative example in Table 2 we present the size distribution (effective radii and effective variance corresponding to a gamma size distribution) retrieved by Tomasko et al. (1999) at Mars Pathfinder surroundings.

## 2.2. Martian dust analogs

### 2.2.1. Origin and refractive indices

In our experiments five different analog samples have been analyzed, namely, two palagonites (JSC0, JSC200), montmorillonite, basalt, and calcite.

Since Mars and the Earth probably were formed at the same time and region of the Solar System, it is logical to find the same elements and minerals on both planets. Therefore, and since there is no available martian dust to perform a laboratory study on Earth, dust analogs must be used. Early choices of Earth spectral analogs showed a predominantly montmorillonite composition since its reflectance spectra in the VIS and NIR are similar to the martian spectra (Toon et al., 1977). Notwithstanding, it appears that the bright soils have a dominant spectral characteristic for terrestrial weathering products of basaltic ash or glass, the palagonites (Crisp et al., 1992; Bell et al., 1993). Palagonites are found to be better spectral martian dust analogs. The montmorillonite spectrum has a greater number of spectral features and higher emissivity in contrast to the palagonite spectrum (Roush and Orenberg, 1996). Both materials are commonly used as terrestrial analogs for bright martian soils (e.g. Banin, 1988; Banin et al., 1988b,a; Orenberg and Handy, 1992).

The palagonite sample used in this study is the <1 mm size fraction of a palagonitic tephra (glassy volcanic ash altered at low temperatures) sample labeled as JSC Mars-1, where JSC stands for Johnson Space Center (Allen et al., 1998). Allen et al. (1997) compare the VIS/NIR spectrum of the JSC Mars-1 simulant to a martian bright region spectrum as measured from the Earth and the ISM Phobos-2 instrument. Both spectra indicate a ferric absorption band in the 800–900 region, and flat absorption in the near-IR. However, the absorption bands at 1400 and 1900 nm in the simulant spectrum indicate a higher level of  $\text{H}_2\text{O}$  and OH in the simulant than on Mars. Then, the original sample was first sieved with a 200  $\mu\text{m}$  sieve to remove the millimeter-sized particles. Subsequently, part of the sample was heated up to 200  $^\circ\text{C}$  and left in the oven for 24 h to get rid of the volatile components. To distinguish the heated and non-heated JSC samples, we call them JSC200 and JSC0, respectively.

Montmorillonite is the dominant clay mineral in bentonite, an altered volcanic ash. The montmorillonite sample used in this work is commercially available from WARD's Science, USA.

Apart from the palagonites and montmorillonite, we also present measurements for a basalt sample collected at Tenerife Island (Canary archipelago, Spain), which corresponds to the 1705 Arenas

Negras volcanic eruption. The lava flow is defined as olivinic-pyroxenic basalt.

Although calcite is not a major component of the martian surface, it is commonly considered to be particularly important for its link with climate evolution and water resources on Mars (Booth and Kieffer, 1978; Gooding, 1978). The calcite sample studied in this work was obtained from limestone bulk material collected near Lecce, Italy (Orofino et al., 1998) and was previously studied by Dabrowska et al. (2013).

The approximate complex refractive indices of the studied samples and corresponding references are given in Table 1. Both the real and imaginary parts of the refractive indices remain essentially constant at visible wavelengths, except for the orange/brown colored JSC0 and JSC200 samples, for which the imaginary part is significantly higher in the blue than in the red region of the spectrum. This is possibly linked to the high iron content of the JSC samples. According to the measured optical constants of silicates of variable iron content, the imaginary part of refractive index increases as the iron content increases (Dorschner et al., 1995). The high absorption at blue wavelengths in comparison with that at red wavelengths of the JSC samples perfectly mimics the behavior of martian dust in the visible (see Table 1 and Fig. 1, right panel).

Basalt is black/gray colored having low iron content compared to that found in the JSC samples. In contrast, calcite and montmorillonite show white and light gray colors, respectively. Calcite is an uni-axial birefringent material, so it has one optical axis and, instead of one refractive index, it has a dielectric tensor specified by two principal dielectric functions, the ordinary,  $n_o$  and extraordinary,  $n_e$  refractive indices. In Table 1 we present the single effective refractive index  $m_{\text{eff}} = ((n_e^2 + n_o^2)/2)^{1/2}$  at the corresponding wavelength (Ghosh, 1999). The imaginary part of the refractive index,  $k$ , is assumed to be zero since pure calcite is very weakly absorbing in the visible.

### 2.2.2. Shapes

Fig. 2 displays the SEM images of basalt (a), palagonite samples JSC0 (b), and JSC200 (c), montmorillonite (d), and calcite (e). At microscopic scales, a variety of geometric forms are present. In particular, the calcite and montmorillonite particles present rhombohedral- and flake-like structures with layered structures typical of sedimentary minerals. We might note that the SEM images are not necessarily representative of the size distribution of each sample. For that purpose we refer the reader to next subsection.

### 2.2.3. Determination of the size distribution of the dust analogs

The size distribution of the martian analog samples is measured using the commercially available Mastersizer 2000 particle sizer from Malvern Instruments. The Mastersizer measures the phase function of the sample at 633 nm in a certain scattering angle range with special attention to the forward scattering peak. It uses either Lorenz–Mie or Fraunhofer diffraction theories to retrieve the volume distributions that best fit the measurements. The retrievals from both methods are simplifications based on the assumption that the particles are spherical. In addition, the Fraunhofer method puts restrictions on the size of the particles since it is only applicable to particles larger than the wavelength of the incident light. However, our martian analog samples contain particles with sizes ranging from sub-micron up to tens of microns. In general, the retrieved effective radii from Lorenz–Mie theory is larger than the corresponding value assuming Fraunhofer theory. Results of both sizing methods tend to converge as the particles become larger. Previous computations seem to indicate that differences between the phase functions derived from Fraunhofer diffraction theory and from Lorenz–Mie theory are significant for size parameters smaller than unity (Veihelmann et al., 2006). Those

**Table 1**

Estimated refractive indices ( $m = n + ik$ ) of our analog samples presented together with the refractive index of martian dust as retrieved by Wolff et al. (2009).

Sample	$m(488 \text{ nm})$	$m(647 \text{ nm})$	Source
Basalt	$1.52 + 0.00092i$	$1.52 + 0.001i$	Pollack et al. (1973)
JSC0/JSC200	$1.5 + 0.01i$	$1.5 + 0.001i$	Clancy et al. (1995)
Montmorillonite	$1.52 + 0.0001i$	$1.52 + 0.0001i$	Sokolik and Toon (1999)
Calcite	$1.6 + 0i$	$1.6 + 0i$	Ghosh (1999)
Martian dust	$1.495 + 0.012 - 0.008$	$1.5 + 0.002 - 0.001$	Wolff et al. (2009)

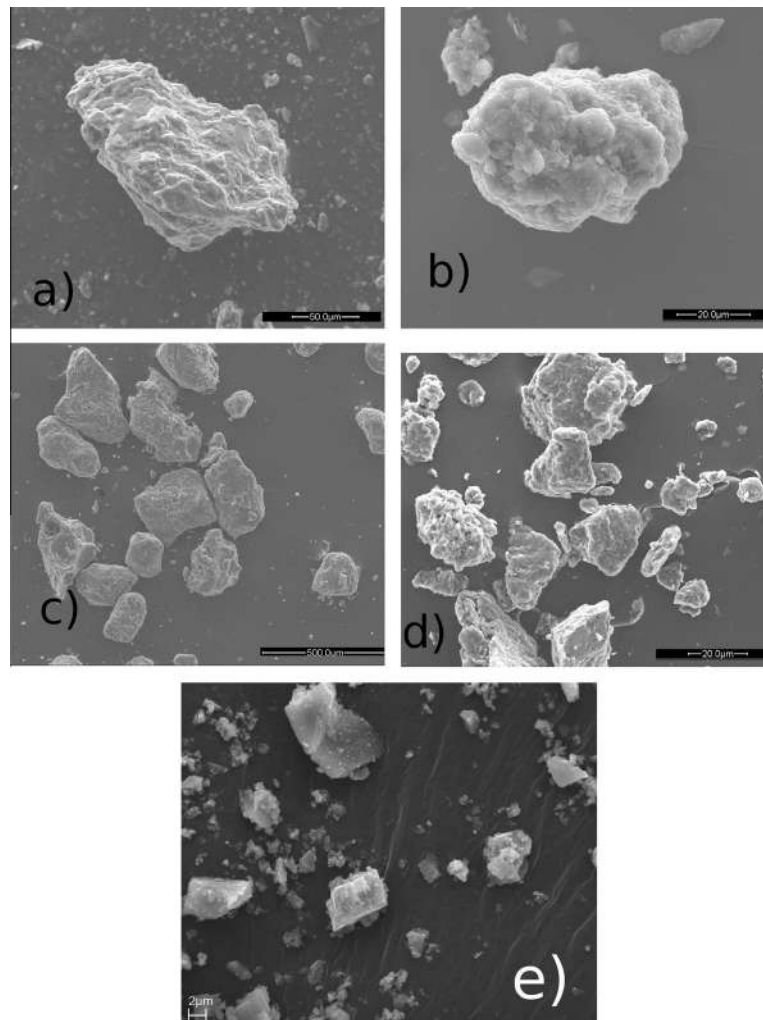


**Fig. 2.** Scanning Electron Microscope images of (a) basalt, (b) JSC0, (c) JSC200, (d) montmorillonite, and (e) calcite. White bars denote the scale of the images.

differences could be responsible for the discrepancies in the retrieved effective radii and variances from both methods. We refer to Erdogan et al. (2007), for a systematic study of the effect of particle irregularity on the retrieved size distributions of diffraction based commercial counters. In this article and in the Amsterdam–Granada Light Scattering Database, <http://www.iaa.es/scattering/> we present both size distributions to facilitate the comparison to other published works where only the Fraunhofer size distribution is available.

Fig. 3 depicts the retrieved number distributions as functions of radius for our samples from both, Fraunhofer (left panel) and Lorenz–Mie (right panel) theories. In those panels,  $r$  represents the radius of a sphere having the same volume as the particle (volume equivalent sphere). The transformation equations to obtain  $n(r)$ , from the measured volume size distribution,  $\nu(r)$  are given at

[http://www.iaa.es/scattering/site\\_media/sizedistributions.pdf](http://www.iaa.es/scattering/site_media/sizedistributions.pdf) (see also Volten et al. (2005)).

From the measured size distributions we calculate the values of the effective radii  $r_{\text{eff}}$  and effective variances  $\nu_{\text{eff}}$  as defined in Eqs. (1) and (2). In Table 2 we present the calculated  $r_{\text{eff}}$  and  $\nu_{\text{eff}}$  for our samples. For a direct comparison with martian dust we also include in Table 2 the values retrieved by Tomasko et al. (1999). As shown, our samples are characterized by a broad range of sizes, having, in many cases,  $r_{\text{eff}}$  and  $\nu_{\text{eff}}$  higher than those retrieved by Tomasko et al. (1999) for martian dust. However, it must be noted that the dust size distribution in the martian atmosphere surely depends strongly on the weather conditions and altitude as already stated. In addition, our goal is to determine how the different physical parameters of our martian dust analogs might affect the measured scattering matrices.

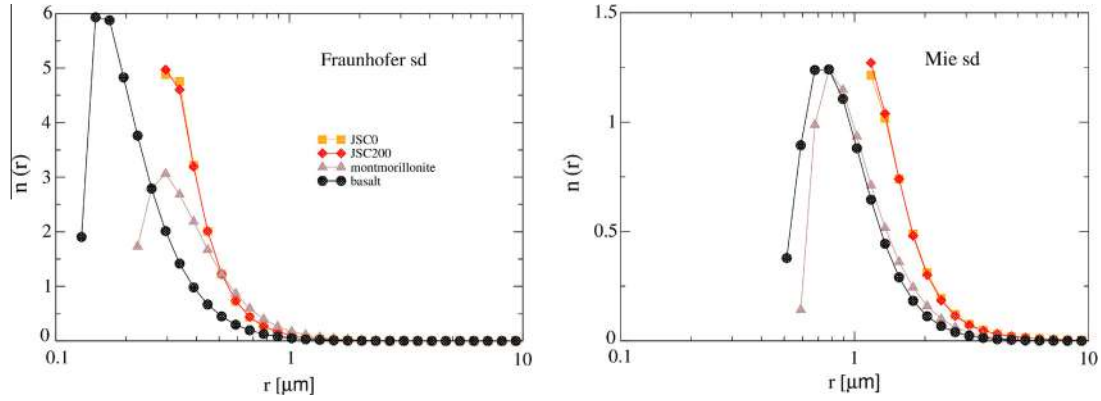


**Fig. 3.** Number,  $n(r)$ , distributions of the basalt (circles), JSC0 (squares), JSC200 (diamonds) and montmorillonite (triangles) samples as measured by Mastersizer 2000 from Malvern Instruments, based either on Fraunhofer (left) or Lorenz–Mie (right panels) theories.

**Table 2**

Effective radii  $r_{\text{eff}}$  and effective variances  $v_{\text{eff}}$  retrieved from the measured Fraunhofer and Mie size distributions.

Sample	Method	$r_{\text{eff}}$ ( $\mu\text{m}$ )	$v_{\text{eff}}$
Basalt	Fraunhofer	2.9	15.1
	Lorenz–Mie	6.9	7.0
JSC0	Fraunhofer	17.2	2.4
	Lorenz–Mie	29.5	1.1
JSC200	Fraunhofer	15.5	2.8
	Lorenz–Mie	28.1	1.2
Calcite	Fraunhofer	1.7	7.6
	Lorenz–Mie	3.3	4.9
Montmorillonite	Fraunhofer	1.8	1.6
	Lorenz–Mie	2.8	1.2
Martian dust	Tomasko et al. (1999)	$1.6 \pm 0.15$	0.2–0.5 or more

### 3. Experimental apparatus

The scattering matrices of our samples are measured at the IAA Cosmic DUst LABORatory (CODULAB) located at the Instituto de Astrofísica de Andalucía, Granada, Spain. In this section we give a brief description of the experimental apparatus. For a detailed description of the experimental apparatus, calibration process, and data acquisition we refer to Muñoz et al. (2010).

The IAA CODULAB is designed to study dust particles in the size range between 0.1  $\mu\text{m}$  and 100  $\mu\text{m}$  (in radius). We use an Argon–Krypton laser as light source that can emits at five different wavelengths. In this work we present measurements at two wavelengths, namely: 488 and 647 nm. The laser beam passes through a polarizer and an electro-optic modulator. The modulated light is subsequently scattered by an ensemble of randomly oriented dust particles located in a jet stream produced by an aerosol generator. The scattered light passes through a quarter-wave plate and an analyzer (both optional) and is detected by a photomultiplier tube which moves along a ring. In this way a range of scattering angles from 3° to 177° is covered in the measurements. Another photomultiplier tube located at a fixed position is used to correct from fluctuations of the signal. We employ polarization modulation in combination with lock-in detection to obtain the entire four-by-four scattering matrix up to a constant. By using eight different combinations of the optical components and their orientations, and assuming the reciprocity of the sample (in particular  $F_{21}/F_{11} = F_{12}/F_{11}$ ,  $F_{31}/F_{11} = -F_{13}/F_{11}$  and  $F_{41}/F_{11} = F_{14}/F_{11}$ ), all scattering matrix elements are obtained as functions of the scattering angle (Hovenier, 2000; Muñoz et al., 2010).

All matrix elements (except  $F_{11}$  itself) are normalized to  $F_{11}$ , that is, we consider  $F_{ij}/F_{11}$ , with  $i, j = 1$  to 4 with the exception

of  $i = j = 1$ . The values of  $F_{11}(\theta)$  are normalized so that they are equal to 1 at  $\theta = 30^\circ$ . The function  $F_{11}(\theta)$ , normalized in this way, is called the phase function or scattering function in this paper.

The reliability of the apparatus has been tested by comparing measured scattering matrices of spherical water droplets at 488 nm, 520 nm and 647 nm with Lorenz–Mie computations (Muñoz et al., 2010). In addition, special tests have been performed to ensure that our experiment is performed under the single scattering regime (Muñoz et al., 2011). We also check that the measurements fulfill the Cloude coherency matrix test given in Hovenier et al. (1986) within the experimental errors at all measured scattering angles.

### 4. Results

In Section 4.1 we present the experimentally determined scattering matrices for the five martian dust analog samples described in Section 2. The measured scattering matrices are compared with Lorenz–Mie calculations for spheres with the same number distributions and refractive index as our sample have. In Section 4.2 we describe how we construct a synthetic scattering matrix in the full range from 0° to 180° scattering angles, and derive the asymmetry parameters for our samples.

#### 4.1. Measured scattering matrices

In Figs. 4–7, we present the measured scattering matrix elements as functions of the scattering angle for the JSC0, JSC200, calcite, basalt (488 and 647 nm), and montmorillonite (488 nm) samples. The measurements cover the scattering angle range from 3° to 177°. We note that the measured scattering matrix at 647 nm for the calcite sample has been previously published by Dabrowska et al. (2013). We refrain from showing the elements  $F_{13}(\theta)/F_{11}(\theta)$ ,  $F_{14}(\theta)/F_{11}(\theta)$ ,  $F_{23}(\theta)/F_{11}(\theta)$ , and  $F_{24}(\theta)/F_{11}(\theta)$ , since they were found to be zero over the entire angle range within the accuracy of the measurements. This agrees with the assumption of randomly oriented particles with equal amounts of particles and their mirror particles (van de Hulst, 1981). All phase functions,  $F_{11}(\theta)$ , are arbitrarily normalized to 1° at 30° scattering angle, and always shown on a logarithmic scale. The experimental errors are indicated by error bars. When no error bar appears, this is because the experimental error is smaller than the symbol plotted. In general, the measurements for the JSC samples show larger error bars than the measurements for all the other samples. This is predominantly due to the fact that those particles are relatively large so that relatively few particles are present in the scattering volume

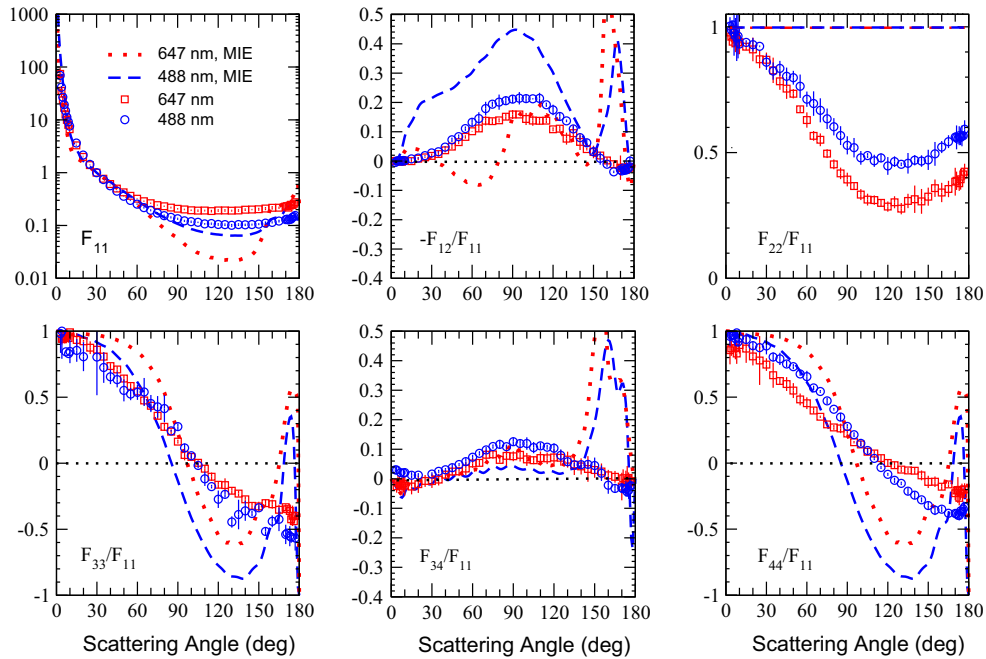


**Fig. 4.** Measured scattering matrix elements as functions of the scattering angle at 488 (circles) and 647 nm (squares) for the JSC0 sample. Dashed and dotted lines correspond to Lorenz–Mie calculations for spheres at 488 and 647 nm, respectively. For the Lorenz–Mie calculations we have used the same size distribution (Mie) and refractive index as the JSC0 sample.

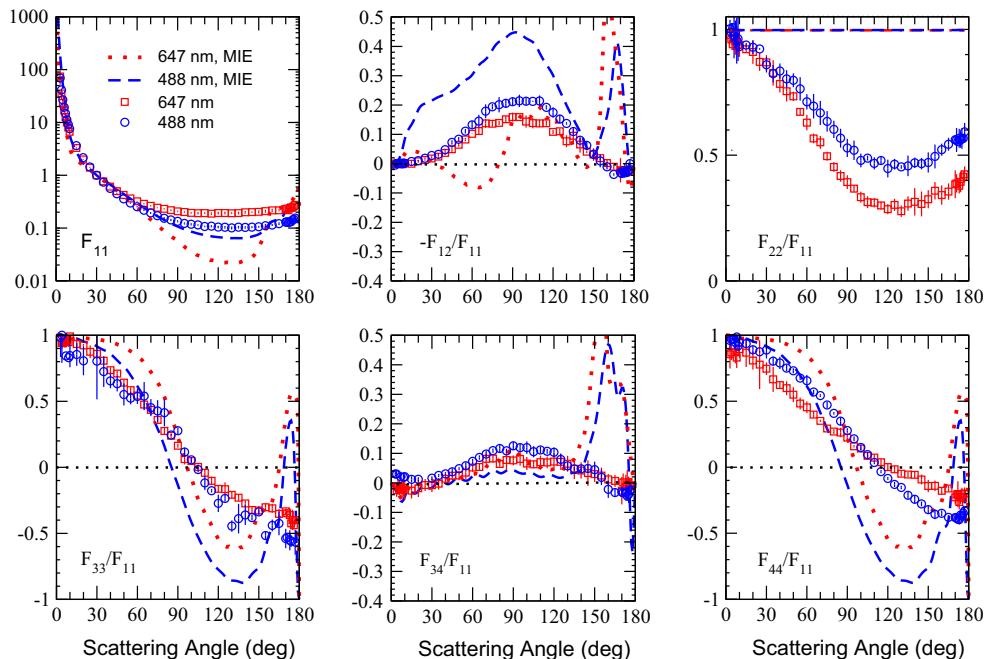


**Fig. 5.** Same as Fig. 4 but for the JSC200 sample.

during the measurements, thereby decreasing the signal-to-noise ratio.

It is interesting to note that small differences in the physical properties of the JSC0 and JSC200 samples (e.g. size distribution) do not produce any significant effect on the measured scattering matrix elements.

In all studied cases, the measured phase function,  $F_{11}(\theta)$ , presents the typical behavior for irregular mineral dust, i.e. it is a smooth function of scattering angle with steep forward peak and

practically no structure at side- and back-scattering angles (see e.g. Muñoz et al., 2000, 2012; Volten et al., 2005).

The measured degree of linear polarization for incident unpolarized light,  $-F_{12}(\theta)/F_{11}(\theta)$ , displays the well-known bell shape in all cases, with a maximum at side-scattering angles, and a negative branch near back-scattering. Table 3 presents the measured main parameters in the region of minimum polarization ( $(-F_{12}/F_{11})_{min}$ ,  $\theta_{min}$ ), inversion ( $\theta_{inv}$ ), and maximum polarization ( $(-F_{12}/F_{11})_{max}$ ,  $\theta_{max}$ ), at the two studied wavelengths.

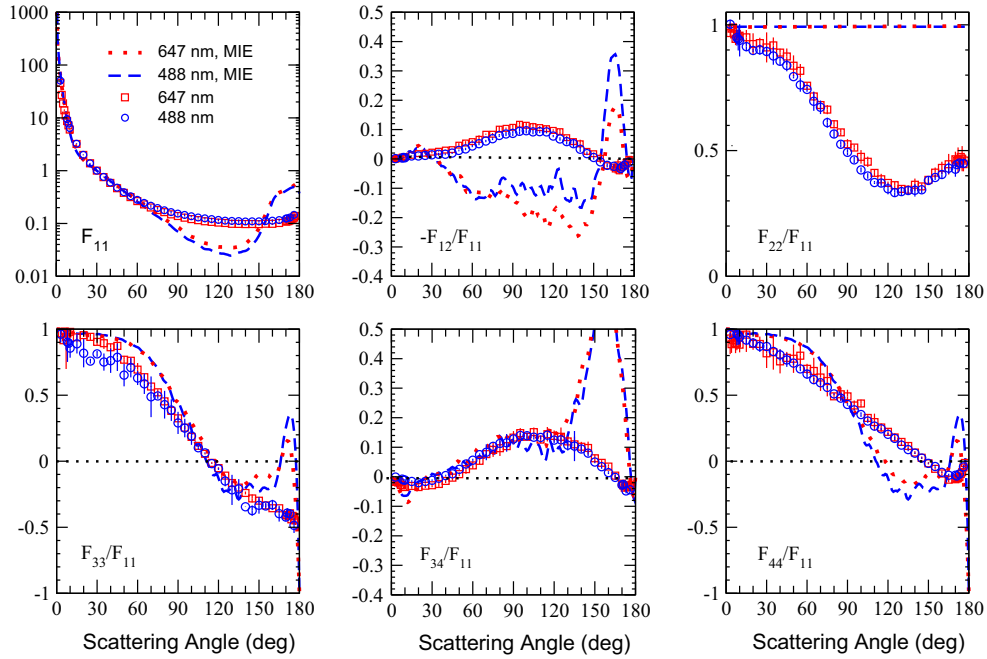


Fig. 6. Same as Fig. 4 but for the basalt sample.

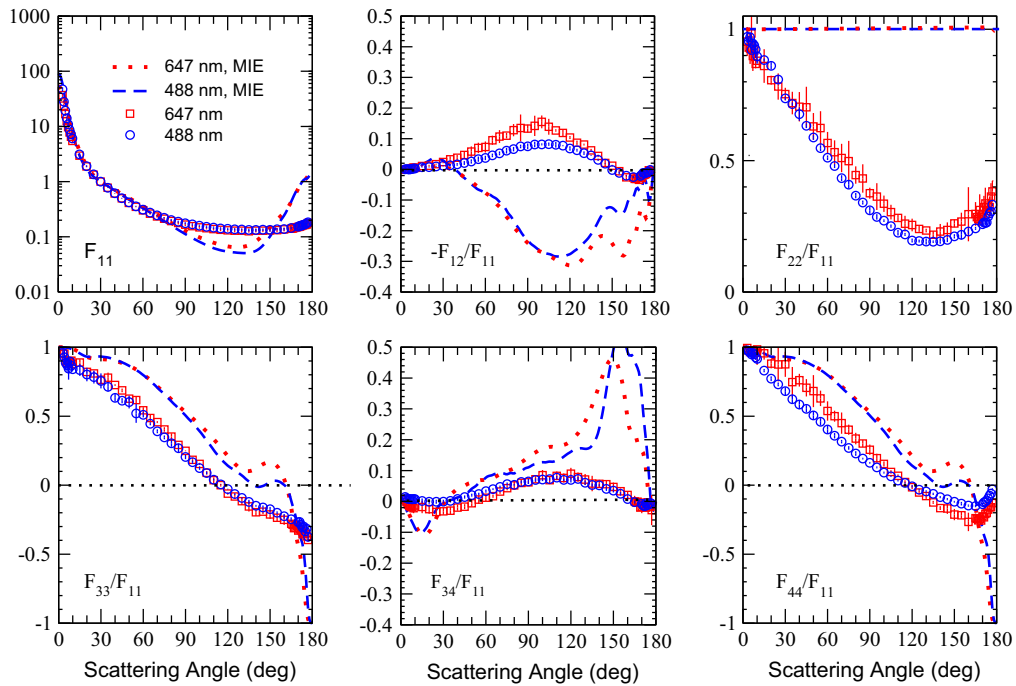


Fig. 7. Same as Fig. 4 but for the calcite sample. The measurements at 647 nm have been previously published by Dabrowska et al. (2013).

In Fig. 9, we compare the  $-F_{12}(\theta)/F_{11}(\theta)$  ratio at 488 nm (top) and 647 nm (bottom) for the 5 martian dust analog samples. As shown, while for red wavelengths the maxima of the  $-F_{12}(\theta)/F_{11}(\theta)$  are similar for all samples, in the blue region the JSC samples are those having higher maxima relative to all the other samples. This is a very important result, coincidentally, those JSC samples are the ones having the largest effective radii. However, we conclude that it must be a consequence of the dominating effect of the much higher imaginary refractive index in those JSC samples as previous computations with irregular particles seem to indicate Zubko et al. (2011).

Moreover, it is interesting to note that the maximum of the  $-F_{12}(\theta)/F_{11}(\theta)$  ratio,  $((-F_{12}/F_{11})_{max})$ , for basalt, montmorillonite, and calcite samples, show higher values at 647 nm than at 488 nm i.e. they present a red polarization color (see Table 3). That seems to be also the color for silicate-type samples with low iron content as shown in many of the samples presented in the Amsterdam–Granada Light Scattering Database (Muñoz et al., 2012). As presented in Table 1, the imaginary part of the refractive index of the mentioned samples show a flat wavelength dependence. However, the JSC0 and JSC200 that present a significantly higher imaginary part of the refractive index at 488 nm than at 647 nm

**Table 3**  
Measured maxima and minima of the degree of linear polarization for unpolarized incident light and the corresponding scattering angles at which they are obtained. We also present the inversion angle for all studied samples together with the inversion angle for martian (yellow) dust clouds as measured by Ebisawa and Dollfus (1993).

Sample	$\lambda$ (nm)	$(-F_{12}/F_{11})_{min}$	$\theta_{min}$ (°)	$(-F_{12}/F_{11})_{max}$	$\theta_{max}$ (°)	$\theta_{inv}$ (°)
JSCO	488	$-0.037 \pm 0.021$	$172 \pm 1$	$0.21 \pm 0.02$	$100 \pm 5$	$155 \pm 5$
	647	$-0.036 \pm 0.017$	$174 \pm 1$	$0.14 \pm 0.01$	$90 \pm 5$	$155 \pm 5$
JSC200	488	$-0.031 \pm 0.013$	$174 \pm 1$	$0.21 \pm 0.02$	$95 \pm 5$	$155 \pm 5$
	647	$-0.054 \pm 0.09$	$172 \pm 1$	$0.159 \pm 0.015$	$90 \pm 5$	$160 \pm 5$
Mont-morillonite	488	$-0.024 \pm 0.018$	$172 \pm 1$	$0.104 \pm 0.001$	$70 \pm 5$	$15 \pm 55$
Basalt	488	$-0.033 \pm 0.01$	$170 \pm 1$	$0.096 \pm 0.009$	$100 \pm 5$	$150 \pm 5$
	647	$-0.03 \pm 0.008$	$170 \pm 1$	$0.12 \pm 0.01$	$95 \pm 5$	$155 \pm 5$
Calcite	488	$-0.025 \pm 0.003$	$165 \pm 5$	$0.082 \pm 0.005$	$105 \pm 5$	$150 \pm 5$
	647	$-0.034 \pm 0.008$	$169 \pm 1$	$0.155 \pm 0.021$	$100 \pm 5$	$150 \pm 5$
Martian clouds	590	$-0.007$	165			152

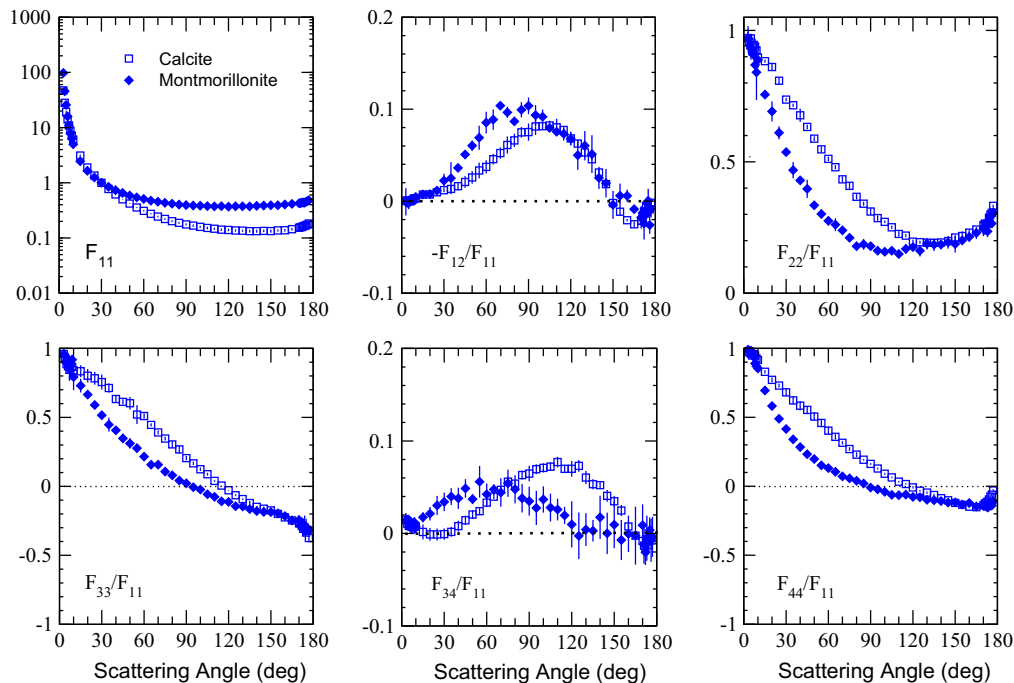


**Fig. 8.** Measured scattering matrix elements as functions of the scattering angle at for the montmorillonite (diamonds) and calcite (squares) samples at 488 nm.

show a blue polarization color. Thus, since different martian analogs have clearly different, wavelength-dependent polarimetric behavior, this could be used as a diagnostic tool to infer the composition of the dust.

The  $F_{22}(\theta)/F_{11}(\theta)$  ratio is often used as an indication of the nonsphericity of the particles, since for optically inactive spheres equals unity at all scattering angles. This ratio is affected by both the size distribution and refractive indices of the samples. In particular, we obtain for the most absorbing samples (JSCO and JSC200), a wavelength dependence opposite to all the other samples, which agrees with the results by Volten et al. (2001).

The ratio  $F_{33}(\theta)/F_{11}(\theta)$ , is found to be different from the  $F_{44}(\theta)/F_{11}(\theta)$  at nearly all measured scattering angles, with  $F_{44}/F_{11}(\theta) > F_{33}/F_{11}(\theta)$  at back-scattering angles. As indicated by Mishchenko et al. (2000) and shown in many examples in the Amsterdam–Granada Light Scattering Database, this is a general property for irregular dust particles.

The pattern for the  $F_{34}(\theta)/F_{11}(\theta)$  ratio is very similar for all studied samples with a maximum at side-scattering angles and two negative branches at small and large scattering angles.

In Fig. 8 we compare the scattering matrices for montmorillonite and calcite samples at 488 nm. As shown in Table 1, the refractive index of both samples do not differ very much and their

effective radii (see Table 2) and shapes are nearly identical (Section 2.2). However, the calcite sample has a  $\nu_{eff}$  equal to 7.6 (Fraunhofer theory), whereas the montmorillonite shows a  $\nu_{eff}$  equal to 1.6 (Fraunhofer theory). Therefore, any differences in their scattering behavior are most likely due to the differences in the width of their size distributions.

In particular, the maximum of the  $-F_{12}(\theta)/F_{11}(\theta)$  and  $F_{34}(\theta)/F_{11}(\theta)$  ratios for montmorillonite are moved toward smaller scattering angles. Moreover, the  $F_{22}(\theta)/F_{11}(\theta)$ ,  $F_{33}(\theta)/F_{11}(\theta)$  and  $F_{44}(\theta)/F_{11}(\theta)$  for montmorillonite show significantly smaller values at forward- and side-scattering angles than those presented by the calcite sample. This seems to indicate that the effective variance of the size distribution may have a significant effect in nearly all scattering matrix elements.

#### 4.2. Lorenz–Mie calculations versus measured scattering matrices

In Figs. 4–7, we compare the measured scattering matrix elements as functions of the scattering angle with results of Lorenz–Mie theory for homogeneous optically non-active spherical particles. For the Lorenz–Mie calculations we employ the number distribution and refractive index of the corresponding sample. The calculated phase function are also normalized to  $1^\circ$  at  $30^\circ$ .

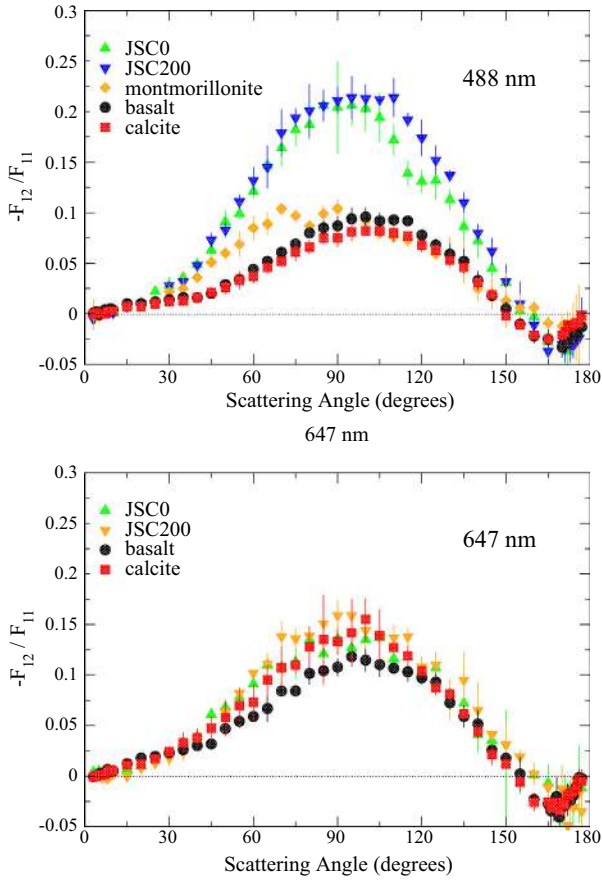


**Fig. 9.** Measured degree of linear polarization as function of the scattering angle for the JSC0 (triangles), JSC200 (triangles down), montmorillonite (diamonds), basalt (circles), and calcite (squares) at 488 nm (top panel) and 647 nm (bottom panel).

**Table 4**

The asymmetry parameter,  $g$ , retrieved from the synthetic phase functions,  $F_{11}^{au}$  of our analog samples at 488 and 647 nm. Values for martian dust are obtained from Ockert-Bell et al. (1997).

Sample	$g$ (488 nm)		$g$ (647 nm)	
	Fr sd	Mie sd	Fr sd	Mie sd
Basalt	0.65	0.74	0.65	0.71
JSC0	0.67	0.80	0.53	0.64
JSC200	0.73	0.84	0.58	0.68
Calcite	0.61	0.65	0.60	0.63
Montmorillonite	0.44	0.51		
Martian dust	0.84 (400 nm)		0.65 (700 nm)	

As it has been previously demonstrated (e.g. Muñoz et al., 2004), the scattering pattern for spherical particles cannot be used to represent the real behavior of natural, irregularly-shaped dust particles. In particular, the relative differences between calculated and experimental phase functions are quite strong at side- and back-scattering angles. Moreover, the measured degree of linear polarization for incident unpolarized light shows positive values at nearly all scattering angles with a maximum in the 90–100° region and a negative branch at backward direction. As mentioned, that is a typical behavior for irregular mineral dust as shown in many examples at the Amsterdam–Granada Light Scattering Database. In contrast, the calculated values tend to be negative at almost all scattering angles with exception of the JSC0 and JSC200 samples. Moreover, the  $F_{22}(\theta)/F_{11}(\theta)$  is equal to 1 at all scattering angles for spherical particles while the measured results for our

martian dust analogs strongly deviate from 1 at nearly all measured scattering angles. Significant differences between calculated and measured values are also found for the other elements of the scattering matrix.

#### 4.3. Synthetic scattering matrices

As mentioned, the experimental measurements do not cover either forward scattering or the exact backward scattering directions. Therefore, what we obtain is the relative phase function,  $F_{11}(\theta)/F_{11}(30^\circ)$ , where (see Volten et al., 2006),

$$\frac{F_{11}(\theta)}{F_{11}(30^\circ)} = \frac{F_{11}^{au}(\theta)}{F_{11}^{au}(30^\circ)}. \quad (3)$$

The  $F_{11}^{au}(\theta)$  ratio is the auxiliary phase function which is normalized the way its average over all directions equals unity, i.e.,

$$1/2 \int_0^\pi d\theta \sin\theta F_{11}^{au}(\theta) = 1. \quad (4)$$

The lack of measurements at forward and back-scattering angles limits the use of the measured scattering matrix data for radiative transfer calculations. To facilitate the use of the experimental data we construct the so-called synthetic scattering matrices from our measurements. Then, the matrices are defined in the full scattering angle range, from 0° to 180°.

The extrapolation of the phase function,  $F_{11}(\theta)$  is based on the assumption that the forward diffraction peak for randomly oriented particles with moderate aspect ratios mainly depends on the size of the particles and is largely independent of their shape (Liu et al., 2003). Thus we merge the results of Lorenz–Mie calculations for projected-surface-area equivalent spheres between 0° and 3° with the corresponding measured phase function. For the Lorenz–Mie computations we use the measured size distribution retrieved from both Fraunhofer and Lorenz–Mie theories (Fig. 3) and assuming the particles to have a refractive indices as given in Table 1. In the case of calcite, the effective refractive index,  $m_{\text{eff}} = 1.6 + 0.0i$  is considered (Dabrowska et al., 2013). For all samples the scaled phase functions, are then extrapolated to 180° assuming a smooth polynomial extrapolation. Once the phase functions are defined in the full range from 0° to 180°, we check whether the normalization condition (Eq. 4) is satisfied. If that is not the case, the measured point at the overlap angle (in our case 3°) is iteratively adjusted until the normalization condition is satisfied.

From the extrapolated phase functions,  $F_{11}^{au}$ , we compute the asymmetry parameter  $g$ , defined as follows:

$$g = \int_0^\pi d\theta \sin\theta \cos\theta F_{11}^{au}(\theta). \quad (5)$$

The computed values for our martian dust analogs are presented in Table 4.

For the relative scattering matrix elements,  $F_{ij}(\theta)/F_{11}(\theta)$  (where  $i, j = 1..4$ , and  $i \neq j \neq 1$ ), a polynomial extrapolation is used for both forward and backward scattering directions. Values at exact forward and backward scattering were determined so that they satisfy the conditions given by Hovenier and van der Mee (2000). In addition, we make use of the fact that for each element of the scattering matrix the right-hand derivative at 0° scattering angle and the left-hand derivative at 180° must both vanish as described by Hovenier and Guirado (2014).

Tables with the experimental data and the corresponding extrapolated matrices for all samples are freely available at the Amsterdam–Granada Light Scattering Database <http://www.iaa.es/scattering/> under the request of citation of this paper and Muñoz et al. (2012).

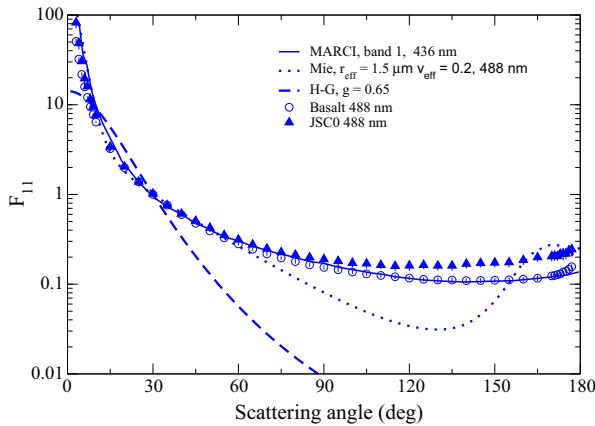


**Fig. 10.** Pseudo emission phase function constructed from MARCI band 1 Wolff et al. (2010) at 436 nm (solid line) (top). We also present the analytical Henyey–Greenstein phase function for  $g = 0.65$  (dashed line), and calculated phase functions for spheres (dotted line) together with our measurements for basalt, and JSCO samples at 488 nm.

## 5. Comparison with derived phase functions and degree of linear polarization in the martian atmosphere

In Figs. 10 and 11, we show the pseudo emission phase function retrieved from the Mars Colors Imager (MARCI band1) on board the Mars Reconnaissance Orbiter (MRO) observations (Wolff et al., 2009) and data of the imager for Mars Pathfinder at 671 nm (Tomasko et al., 1999), respectively. In particular, we show the retrieved phase function at 671 nm, corresponding to a gamma size distributions with  $r_{\text{eff}}$  equal to  $1.6 \mu\text{m}$  and  $v_{\text{eff}}$  equal to 0.2. The observations for martian dust are presented together with Lorenz–Mie calculations for the same size distribution as retrieved by Tomasko et al. (1999) and the refractive indices of the JSC sample (Table 1). Moreover, we show single Henyey–Greenstein phase functions for the asymmetry parameters retrieved for martian dust at the corresponding wavelengths, namely  $g = 0.65$  at blue wavelengths and  $g = 0.75$  at red wavelengths (Ockert-Bell et al., 1997), together with the experimental phase functions for the martian dust analogs is remarkable, especially in the case of the basalt sample at both wavelengths. To facilitate comparison with the laboratory measurements, in all cases the phase function is normalized to unity at  $30^\circ$ .

As can be seen, none of the computed phase functions reproduce the observations for Mars. On the contrary, despite the differences in the size distributions of the martian dust derived by Tomasko et al. (1999) and our martian dust analogs, the agreement between observed and experimental phase functions for the martian dust analogs is remarkable, especially in the case of the basalt sample at both wavelengths. The main discrepancies are related to the forward diffraction peak that is highly dependent on the size of the particles.

In addition to the  $F_{11}(\theta)$  element, some observations of the degree of linear polarization for incident unpolarized light have also been performed on Mars. A recent review on polarimetry of terrestrial planets has been reported by Kaydash et al. (2015). The limitation of the observations, particularly related to remote measurements from Earth (e.g. Ebisawa and Dollfus, 1993), or near-Earth orbiters like HST (Shkuratov et al., 2005), is that the phase angles available are always restricted to the  $0\text{--}45^\circ$  range. Where the phase and scattering angles are related as:  $\alpha = 180^\circ - \theta$ . Moreover, all observations refer to the atmosphere plus surface system. In case the observations are performed during a dust storm, the contribution of the surface becomes negligible. However, in that case, the contribution of multiple scattering becomes important.

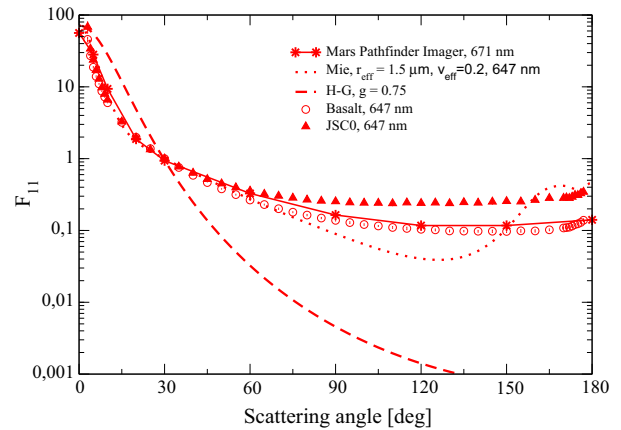


**Fig. 11.** Phase function as derived by Tomasko et al. (1999) at 671 nm. We also present the analytical Henyey–Greenstein phase functions for  $g = 0.75$  (dashed line), and calculated phase functions for spheres (dotted) together with our measurements for basalt, and JSCO samples at 647 nm.

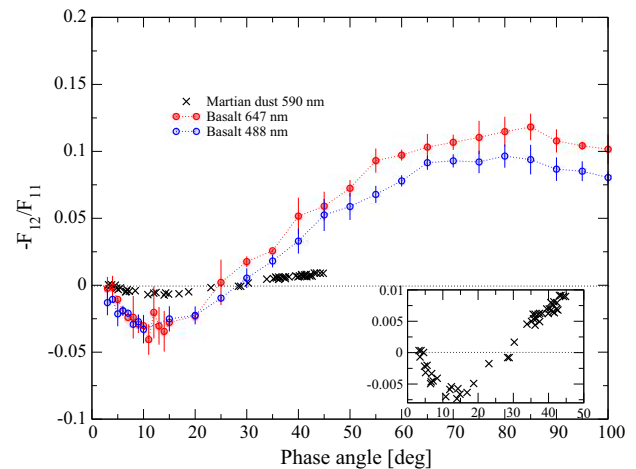


**Fig. 12.** The negative polarization branch of martian dust clouds as observed by Ebisawa and Dollfus (1993) at 590 nm (crosses) presented together with the measured degree of linear polarization for the basalt samples at 488 nm (open dots) and 647 nm (filled dots).

An important characteristic of the  $-F_{12}(\theta)/F_{11}(\theta)$  curve is the inversion angle, which is the scattering angle at which the  $-F_{12}/F_{11} = 0$ , changing from a positive to a negative value. It is generally found in the  $150\text{--}160^\circ$  scattering angle range. As an illustrative example, in Fig. 12 we present our measured  $-F_{12}(\theta)/F_{11}(\theta)$  for basalt at 488 and 647 nm. The experimental data are presented together with martian polarimetric observations described in Ebisawa and Dollfus (1993) at 590 nm, from previous works of Dollfus et al. (1984b,a), corresponding to dust storm conditions. It is seen that the inversion angles of the martian analog samples (see Table 3) closely agree with the martian dust observations indicating an inversion at  $28^\circ$  phase angle. However, the negative branch is much deeper for the laboratory measurements. That seems to be a multiple scattering effect as previous comparative measurements of the phase angle dependence of the degree of linear polarization of particulate surfaces and particles in air show (Shkuratov et al., 2004, 2007).

## 6. Conclusions

We present measurements of the full  $4 \times 4$  scattering matrices as functions of the scattering angle of five martian dust analogs:

basalt, two JSC-1 martian stimulants, montmorillonite, and calcite. To facilitate the use of the experimental scattering matrices for multiple-scattering calculations, we have obtained synthetic scattering matrices based on the measurements in the full scattering angle range from  $0^\circ$  to  $180^\circ$ . Tables of the measured and synthetic scattering matrices are available in the Amsterdam–Granada Light Scattering Database ([www.iaa.es/scattering](http://www.iaa.es/scattering)). The data are freely available under request of citation of this paper and [Muñoz et al. \(2012\)](#).

The measured scattering matrices are compared with results of Lorenz–Mie calculations for the same number distribution and refractive indices as given for our martian dust analogs. The experimental scattering matrices are poorly represented by the Lorenz–Mie calculations, showing strong differences between measured and calculated values at all measured scattering angles. Further, our measured phase functions have been compared with the retrieved phase functions for martian dust from MARCI ([Wolff et al., 2010](#)) and Mars Pathfinder ([Tomasko et al., 1999](#)), analytical Henyey–Greenstein phase functions. The measured phase functions at blue and red wavelengths of the martian analogs closely mimic the phase functions retrieved using space-borne instrumentation ([Wolff et al., 2010](#); [Tomasko et al., 1999](#)). The measured  $-F_{12}(\theta)/F_{11}(\theta)$  ratio show a similar behavior to that observed in Mars during a martian dust storm ([Ebisawa and Dollfus, 1993](#)).

The scattering pattern of the martian analogs follows generally the trend found in previous analysis of other mineral samples (e.g. [Volten et al., 2001](#)). Further, the polarimetric color might be an indication of the composition of martian dust. The measured degree of linear polarization seems to be sensitive to the width of the size distribution. Therefore, spectro-polarimetric observations from martian surface appear to be a powerful diagnostic tool to infer information on the physical properties of martian dust.

Due to the complicated shapes of martian dust, computations for realistic polydisperse irregular particles have to be replaced by simplified models such as cylinders ([Wolff et al., 2006, 2010](#)), spheroids ([Petrova \(1999\)](#)), ellipsoids ([Merikallio et al. \(2013\)](#)), or more sophisticated particles as aggregates of spheres and cubes ([Pitman et al., 2014](#)). Our experimental data can be used to check the validity of such model particles.

In particular, as our measurements indicate:

- Phase functions must be smooth functions of the scattering angle with strong forward peaks and nearly no structure at side- and back-scattering angles.
- The polarization color is directly dependent on the refractive index of the particles showing a red polarization color those particles with a flat dependence of the imaginary part of the refractive index at visible wavelengths and blue polarization color if it is significantly higher at blue than at red wavelengths.
- The maximum of the degree of linear polarization is also strongly dependent on the imaginary part of the refractive index showing highest values for those samples with a higher imaginary part of the refractive index (see e.g. [Zubko et al., 2013](#)).
- Differences in the effective variance of the size distribution of the sample may have a significant effect in the scattering matrix elements.

Once the model is tested, further calculations can be performed at different wavelengths or physical parameters of the particles are which the measurements are not possible.

## Acknowledgments

The SEM pictures were taken at the Scientific Instrumentation Center of the University of Granada. We are indebted to

I. Guerra-Tschuschke for her support with the SEM. This work has been supported by the Plan Nacional de Astronomía y Astrofísica under Contracts AYA2009-08190 and AYA2012-39691, and Junta de Andalucía under Contract P09-FMQ-455.

## References

- Allen, C.C., Morris, R.V., Lindstrom, D.J., Lindstrom, M.M., Lockwood, J.P., 1997. JSC Mars-1 – Martian regolith simulant. *Lunar Planet. Sci.* 28, p. 27.
- Allen, C.C., et al., 1998. Martian regolith simulant JSC Mars-1. *Lunar Planet. Sci.* 29, p. 1690.
- Banin, A., 1988. The soils of Mars. In: Drake, M.J., Greeley, R., McKay, G.A., Blanchard, D.P., Carr, M.H., Gooding, J., McKay, C.P., Spudis, P.D., Squyres, S.W. (Eds.), *Mars Sample Return Science*, pp. 35–36.
- Banin, A., Carle, G.C., Chang, S., Coyne, L.M., Orenberg, J.B., Scattergood, T.W., 1988a. Laboratory investigations of Mars: Chemical and spectroscopic characteristics of a suite of clays as Mars soil analogs. *Origins Life* 18, 239–265.
- Banin, A., et al., 1988b. Constraining Mars soil mineralogical composition: Palagonite vs. iron enriched smectite clays. *Lunar Planet. Sci.* 19, p. 27.
- Bell, J.F., Morris, R.V., Adams, J.B., 1993. Thermally altered palagonitic tephra – A spectral and process analog to the soil and dust of Mars. *J. Geophys. Res.* 98, 3373–3385.
- Booth, M.C., Kieffer, H.H., 1978. Carbonate formation in Marslike environments. *J. Geophys. Res.* 83, 1809–1815.
- Boynton, W.V., et al., 2009. Evidence for calcium carbonate at the phoenix landing site. *Lunar Planet. Sci.* 40, p. 2434.
- Clancy, R.T., Lee, S.W., Gladstone, G.R., McMillan, W.W., Rousch, T., 1995. A new model for Mars atmospheric dust based upon analysis of ultraviolet through infrared observations from Mariner 9, Viking, and PHOBOS. *J. Geophys. Res.* 100, 5251–5263.
- Clancy, R.T., Wolff, M.J., Christensen, P.R., 2003. Mars aerosol studies with the MGS TES emission phase function observations: Optical depths, particle sizes, and ice cloud types versus latitude and solar longitude. *J. Geophys. Res. (Planets)* 108, 5098.
- Crisp, J., Bartholomew, M.J., 1992. Mid-infrared spectroscopy of Pahala ash palagonite and implications for remote sensing studies of Mars. *J. Geophys. Res.* 97, 14691.
- Dabrowska, D.D., Muñoz, O., Moreno, F., Nousiainen, T., Zubko, E., Marra, A.C., 2013. Experimental and simulated scattering matrices of small calcite particles at 647 nm. *J. Quant. Spectrosc. Radiat. Trans.* 124, 62–78.
- de Beule, C., Wurm, G., Kelling, T., Kupper, M., Jankowski, T., Teiser, J., 2014. The martian soil as a planetary gas pump. *Nature Phys.* 10, 17–20.
- Glugach, Z.M., Korabiev, O.I., Morozhenko, A.V., Moroz, V.I., Petrova, E.V., Rodin, A.V., 2003. Physical properties of dust in the martian atmosphere: Analysis of contradictions and possible ways of their resolution. *Solar Syst. Res.* 37, 1–19.
- Dollfus, A., Bowell, E., Ebisawa, S., 1984a. The martian dust storms of 1973 – A polarimetric analysis. *Astron. Astrophys.* 134, 343–353.
- Dollfus, A., Ebisawa, S., Bowell, E., 1984b. Polarimetric analysis of the martian dust storms and clouds in 1971. *Astron. Astrophys.* 131, 123–136.
- Dorschner, J., Begemann, B., Henning, T., Jaeger, C., Mutschke, H., 1995. Steps toward interstellar silicate mineralogy. II. Study of Mg–Fe–silicate glasses of variable composition. *Astron. Astrophys.* 300, 503–520.
- Draine, B.T., Flatau, P.J., 2003. User Guide for the Discrete Dipole Approximation Code DDSCAT.6.0. *ArXiv Astrophysics e-prints*.
- Ebisawa, S., Dollfus, A., 1993. Dust in the martian atmosphere: Polarimetric sensing. *Astron. Astrophys.* 272, 671–686.
- Erdogan, S.T., Garboczi, E.J., Fowler, D.W., 2007. Shape and size of microfine aggregates: X-ray microcomputed tomography vs. laser diffraction. *Powder Technol.* 177, 53–63.
- Ghosh, G., 1999. Dispersion-equation coefficients for the refractive index and birefringence of calcite and quartz crystals. *Opt. Commun.* 163, 95–102.
- Gooding, J.L., 1978. Chemical weathering on Mars – Thermodynamic stabilities of primary minerals/and their alteration products/from mafic igneous rocks. *Icarus* 33, 483–513.
- Hansen, J.E., Travis, L.D., 1974. Light scattering in planetary atmospheres. *Space Sci. Rev.* 16, 527–610.
- Hovenier, J.W., 2000. Measuring scattering matrices of small particles at optical wavelengths. *Light Scatter. Nonspheric. Particles: Theory, Measure. Applicat.*, 355–365.
- Hovenier, J.W., van der Mee, C.V.M., 2000. Basic relationships for matrices describing scattering by small particles. *Light Scatter. Nonspheric. Particles: Theory, Measure. Applicat.*, 61–85.
- Hovenier, J.W., Guirado, D., 2014. Zero slopes of the scattering function and scattering matrix for strict forward and backward scattering by mirror symmetric collections of randomly oriented particles. *J. Quant. Spectrosc. Radiat. Trans.* 133, 596–602.
- Hovenier, J.W., van de Hulst, H.C., van der Mee, C.V.M., 1986. Conditions for the elements of the scattering matrix. *Astron. Astrophys.* 157, 301–310.
- Kahnert, M., 2003. Numerical methods in electromagnetic scattering theory. *J. Quant. Spectrosc. Radiat. Trans.* 79, 775–824.
- Kaydash, V., Shkuratov, Y., Wolff, M., Videen, G., 2015. Polarimetry of terrestrial planets. In: *Polarization of stars and Planetary Systems*. Cambridge University Press (in press).
- Lemmon, M.T. et al., 2004. Atmospheric imaging results from the Mars exploration rovers: Spirit and opportunity. *Science* 306, 1753–1756.

- Liu, L., Mishchenko, M.I., Hovenier, J.W., Volten, H., Muñoz, O., 2003. Scattering matrix of quartz aerosols: Comparison and synthesis of laboratory and Lorenz–Mie results. *J. Quant. Spectrosc. Radiat. Trans.* 79, 911–920.
- Markiewicz, W.J., Sablotny, R.M., Keller, H.U., Thomas, N., Titov, D., Smith, P.H., 1999. Optical properties of the martian aerosols as derived from imager for Mars pathfinder midday sky brightness data. *J. Geophys. Res.* 104, 9009–9018.
- Merikallio, S., Nousiainen, T., Kahnert, M., Harri, A.-M., 2013. Light scattering by the martian dust analog, palagonite, modeled with ellipsoids. *Opt. Express* 21, 17972–17985.
- Mishchenko, M.I., Rossow, W.B., Macke, A., Lacis, A.A., 1996. Sensitivity of cirrus cloud albedo, bidirectional reflectance and optical thickness retrieval accuracy to ice particle shape. *J. Geophys. Res.* 101, 16973.
- Mishchenko, M.I., Wiscombe, W.J., Hovenier, J.W., Travis, L.D., 2000. Overview of scattering by nonspherical particles. *Light Scatter. Nonspheric. Particles: Theory, Measure. Applicat.*, 30–60.
- Moreno, F., Muñoz, O., López-Moreno, J.J., Molina, A., Ortiz, J.L., 2002. A Monte Carlo code to compute energy fluxes in cometary nuclei. *Icarus*.
- Muinenen, K., Nousiainen, T., Lindqvist, H., Muñoz, O., Videen, G., 2009. Light scattering by Gaussian particles with internal inclusions and roughened surfaces using ray optics. *J. Quant. Spectrosc. Radiat. Trans.* 110, 1628–1639.
- Muñoz, O. et al., 2004. Scattering matrices of volcanic ash particles of Mount St. Helens, Redoubt, and Mount Spurr Volcanoes. *J. Geophys. Res. (Atmos.)* 109, 16201.
- Muñoz, O. et al., 2010. Experimental determination of scattering matrices of dust particles at visible wavelengths: The IAA light scattering apparatus. *J. Quant. Spectrosc. Radiat. Trans.* 111, 187–196.
- Muñoz, O., Volten, H., de Haan, J.F., Vassen, W., Hovenier, J.W., 2000. Experimental determination of scattering matrices of olivine and Allende meteorite particles. *Astron. Astrophys.* 360, 777–788.
- Muñoz, O., Moreno, F., Guirado, D., Ramos, J.L., Volten, H., Hovenier, J.W., 2011. The IAA cosmic dust laboratory: Experimental scattering matrices of clay particles. *Icarus* 211, 894–900.
- Muñoz, O., Moreno, F., Guirado, D., Dabrowska, D.D., Volten, H., Hovenier, J.W., 2012. The Amsterdam–Granada Light Scattering Database. *J. Quant. Spectrosc. Radiat. Trans.* 113, 565–574.
- Ockert-Bell, M.E., Bell, J.F., Pollack, J.B., McKay, C.P., Forget, F., 1997. Absorption and scattering properties of the martian dust in the solar wavelengths. *J. Geophys. Res.* 102, 9039–9050.
- Orenberg, J., Handy, J., 1992. Reflectance spectroscopy of palagonite and iron-rich montmorillonite clay mixtures – Implications for the surface composition of Mars. *Icarus* 96, 219–225.
- Orofino, V., Blanco, A., Fonti, S., Proce, R., Rotundi, A., 1998. The infrared optical constants of limestone particles and implications for the search of carbonates on Mars. *Planet. Space Sci.* 46, 1659–1669.
- Petrova, E.V., 1999. Mars aerosol optical thickness retrieved from measurements of the polarization inversion angle and the shape of dust particles. *J. Quant. Spectrosc. Radiat. Trans.* 63, 667–676.
- Pitman, K.M., Wolff, M.J., Cloutis, E.A., 2014. Building more realistic grain shapes in radiative transfer models of Mars regolith. *Lunar Planet. Sci.* 45, p. 2627.
- Pollack, J.B., Toon, O.B., Khare, B.N., 1973. Optical properties of some terrestrial rocks and glasses. *Icarus* 19, 372–389.
- Pollack, J.B., Ockert-Bell, M.E., Shepard, M.K., 1995. Viking lander image analysis of martian atmospheric dust. *J. Geophys. Res.* 100, 5235–5250.
- Poulet, F. et al., 2007. Martian surface mineralogy from observatoire pour la minéralogie, l’Eau, les glaces et l’activité on board the Mars Express spacecraft (OMEGA/MEx): Global mineral maps. *J. Geophys. Res. (Planets)* 112, 8.
- Rannou, P., Perrier, S., Bertaux, J.-L., Montmessin, F., Korabiev, O., Rébérac, A., 2006. Dust and cloud detection at the Mars limb with UV scattered sunlight with SPICAM. *J. Geophys. Res. (Planets)* 111, 9.
- Roush, T.L., Orenberg, J.B., 1996. Estimated detectability limits of iron-substituted montmorillonite clay on Mars from thermal emission spectra of clay–palagonite physical mixtures. *J. Geophys. Res.* 101, 26111–26118.
- Shkuratov, Y., Ovcharenko, A., Zubko, E., Volten, H., Muñoz, O., Videen, G., 2004. The negative polarization of light scattered from particulate surfaces and of independently scattering particles. *J. Quant. Spectrosc. Radiat. Trans.* 88, 267–284.
- Shkuratov, Y., Kreslavsky, M., Kaydash, V., Videen, G., Bell, J., Wolff, M., Hubbard, M., Noll, K., Lubenow, A., 2005. Hubble Space Telescope imaging polarimetry of Mars during the 2003 opposition. *Icarus* 176, 1–11.
- Shkuratov, Y., Bondarenko, S., Kaydash, V., Videen, G., Muñoz, O., Volten, H., 2007. Photometry and polarimetry of particulate surfaces and aerosol particles over a wide range of phase angles. *J. Quant. Spectrosc. Radiat. Trans.* 106, 487–508.
- Smith, P.H. et al., 2009.  $H_2O$  at the phoenix landing site. *Science* 5936, 58–61.
- Sokolik, I.N., Toon, O.B., 1999. Incorporation of mineralogical composition into models of the radiative properties of mineral aerosol from UV to IR wavelengths. *J. Geophys. Res.* 104, 9423–9444.
- Stam, D.M., Hovenier, J.W., 2005. Errors in calculated planetary phase functions and albedos due to neglecting polarization. *Astron. Astrophys.* 444, 275–286.
- Sullivan, R. et al., 2008. Wind-driven particle mobility on Mars: Insights from Mars exploration rover observations at “El Dorado” and surroundings at Gusev Crater. *J. Geophys. Res. (Planets)* 113, 6.
- Taflove, A., Hagness, S., 2005. *Computational Electrodynamics: The Finite-Difference Time-Domain Method*.
- Tomasko, M.G., Doose, L.R., Lemmon, M., Smith, P.H., Wegryn, E., 1999. Properties of dust in the martian atmosphere from the imager on Mars pathfinder. *J. Geophys. Res.* 104, 8987–9008.
- Toon, O.B., Pollack, J.B., Sagan, C., 1977. Physical properties of the particles composing the martian dust storm of 1971–1972. *Icarus* 30, 663–696.
- van de Hulst, H.C., 1981. *Light Scattering by Small Particles*.
- Veihelmann, B., Konert, M., van der Zande, W.J., 2006. Size distribution of mineral aerosol: Using light-scattering models in laser particle sizing. *Appl. Opt.* 45, 6022–6029.
- Volten, H. et al., 2001. Scattering matrices of mineral aerosol particles at 441.6 nm and 632.8 nm. *J. Geophys. Res.* 106, 17375–17402.
- Volten, H. et al., 2005. WWW scattering matrix database for small mineral particles at 441.6 and 632.8 nm. *J. Quant. Spectrosc. Radiat. Trans.* 90, 191–206.
- Volten, H., Muñoz, O., Hovenier, J.W., Waters, L.B.F.M., 2006. An update of the Amsterdam Light Scattering Database. *J. Quant. Spectrosc. Radiat. Trans.* 100, 437–443.
- Wolff, M.J., Clancy, R.T., 2003. Constraints on the size of martian aerosols from thermal emission spectrometer observations. *J. Geophys. Res. (Planets)* 108, 5097.
- Wolff, M.J. et al., 2006. Constraints on dust aerosols from the Mars exploration rovers using MGS overflights and Mini-TES. *J. Geophys. Res. (Planets)* 111, 12.
- Wolff, M.J. et al., 2009. Wavelength dependence of dust aerosol single scattering albedo as observed by the Compact Reconnaissance Imaging Spectrometer. *J. Geophys. Res. (Planets)* 114, 0.
- Wolff, M.J., Todd Clancy, R., Goguen, J.D., Malin, M.C., Cantor, B.A., 2010. Ultraviolet dust aerosol properties as observed by MARCI. *Icarus* 208, 143–155.
- Wriedt, T., 2009. Light scattering theories and computer codes. *J. Quant. Spectrosc. Radiat. Trans.* 110, 833–843.
- Wurm, G., Krauss, O., 2006. Dust eruptions by photophoresis and solid state greenhouse effects. *Phys. Rev. Lett.* 96 (13), 134301–1–134302–4.
- Wurm, G., Teiser, J., Reiss, D., 2008. Greenhouse and thermophoretic effects in dust layers: The missing link for lifting of dust on Mars. *Geophys. Res. Lett.* 35, 10201.
- Yen, A.S., et al., 2013. Evidence for a global martian soil composition extends to gale crater. *Lunar Planet. Sci.* 44, p. 2495.
- Yurkin, M.A., Hoekstra, A.G., 2007. The discrete dipole approximation: An overview and recent developments. *J. Quant. Spectrosc. Radiat. Trans.* 106, 558–589.
- Zubko, E., Videen, G., Shkuratov, Y., Muinenen, K., Yamamoto, T., 2011. The Umov effect for single irregularly shaped particles with sizes comparable with wavelength. *Icarus* 212, 403–415.
- Zubko, E. et al., 2013. Light scattering by feldspar particles: Comparison of model agglomerate debris particles with laboratory samples. *J. Quant. Spectrosc. Radiat. Trans.* 131, 175–187.